ACS NANO

www.acsnano.org

ARTICLE

Roll-to-Roll Flash Joule Heating to Stabilize Electrocatalysts onto Meter-Scale Ni Foam for Advanced Water Splitting

Peng Du, Bohan Deng, Xian He, Wei Zhao, Hongyi Liu, Yuanzheng Long, Zhuting Zhang, Ziwei Li, Kai Huang,* Ke Bi, Ming Lei, and Hui Wu*

Cite This: https://doi.org/10.1021/acsnano.4c13787

Read Online

ACCESS | Metrics & More | Article Recommendations | Supporting Information

ABSTRACT: **The seamless integration of electrocatalysts onto the electrode is crucial for enhancing water electrolyzers, yet it is especially challenging when scaled up to large manufacturing. Despite thorough investigation, there are few reports that tackle this integration through roll-to-roll (R2R) methodology, a technique crucial for fulfilling industrial-scale demands. Here, we develop an R2R flash Joule heating (R2R-FJH) system to process catalytic electrodes with superior performance. The electrodes exhibited improved stability and activity, showcasing an exceptional performance within an alkaline water electrolysis (AWE) system. They achieved a low operation potential of 1.66 V at 0.5 A cm^{-2}, coupled with outstanding durability over the operation of 800 h. We further demonstrated a prototype of a rolled-up water splitting apparatus, illustrating the efficiency of R2R-FJH electrodes in producing high-purity hydrogen through advanced water oxidation. Our study emphasized the practicality and scalability of the R2R-FJH strategy in the industrial manufacturing of high-performance electrodes for water electrolysis.**

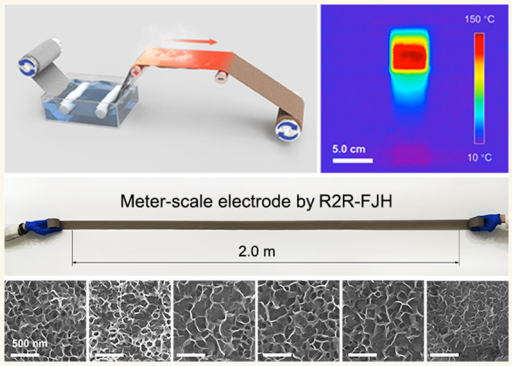

KEYWORDS: *roll-to-roll, flash Joule heating, integrated electrode, water electrolysis, rolled-up electrolyzer*

INTRODUCTION

Electrodes are essential components in water electrolyzers, playing a key role in the production of green hydrogen.[1−6] In a typical industrial 1 MW water electrolyzer stack, the total electrode area for both the oxygen and hydrogen evolution reactions (OER and HER) is around 170 m^2. This demand is rapidly escalating, with projections suggesting it will surpass 20 million m^2 due to an expected surge in global electrolyzer capacity to over 134 GW by 2030.[7−9] Despite significant improvements, current electrode fabrication processes are often inefficient and protracted, constrained by rigorous structural requisites.[10−12] Thus, there is an urgent need for large-scale, efficient fabrication methods for catalytic electrodes that address the increasing requirements of green hydrogen production, ensuring electrochemical efficacy, extended longevity, uniformity, and cost-efficiency. Notably, the roll-to-roll (R2R) process has emerged as a viable approach for large-scale electrode manufacturing, being cost-effective and high-throughput.[13,14] This technique, widely applied in fields like flexible electronics, optics, biomedicine, and sustainable energy, draws from the industrial success of coiled structures in lithium-ion batteries (LIB).[15−18] However, there are limited reports to process high-performance water electrolyzer electrodes in using the R2R methodology, which is imperative for industrial-scale demands.

Therefore, the aspirational balancing between the catalytic performance and scalable manufacturing attracted growing attention in developing water splitting electrodes.[19−21] The efficiency and performance of water electrolyzers depend heavily on the electrocatalysts and how well they are integrated with the electrodes.[22,23] Despite significant efforts to optimize the activity of catalytic layer and substrate mass transport, the challenge of effectively integrating advanced catalyst layers onto electrodes, particularly at high current densities, remains unresolved.[24,25] The industrial focus has been on achieving homogeneity, cost-effectiveness, and scalability in high-performance electrodes without compromising functionality.[26−28] Generally, conventional thermochemical reactions, often employed for growing

Received: September 30, 2024
Revised: December 17, 2024
Accepted: December 23, 2024

electrocatalysts on porous substrates, are conducted under equilibrium-state conditions for controlled composition and morphology.[29,30] However, these processes face scale limitations due to specific duration needs and heat-transfer mechanisms. Alternatively, advancements in controllable Joule heating techniques present a promising solution, with conductive electrode substrates offering distinct reaction rates and thermal properties compared to traditional methods.[31−34] The flash Joule heating strategy, for instance, has shown potential in enhancing the surface binding strength and thermal stability of nanostructures on substrates.[35−37] Yet, existing reactors typically involve small-scale, noncontinuous thermal transients, leading to products unsuitable for large applications.[38,39] Moreover, the chemical compositions are heavily influenced by slight variation of reaction subjects and precise electrical parameter adjustments, posing challenges in practical fabrication.[40,41] In this context, few attempts have been made to combine continuous processing and Joule heating or integrate variations of existing techniques. This approach explores the potential of macrofabrication in overcoming the limitations associated with small-scale, intermittent systems.

We propose that the combination of R2R strategies with flash Joule heating treatment could bridge the gap between controlled modulation and scalable production demands, introducing innovative concepts for electrode production in water electrolysis. Herein, we report a roll-to-roll flash Joule heating (R2R-FJH) strategy utilizing a distinctive configuration to stabilize catalysts onto meter-scale electrodes toward advanced water splitting. A wide range of electrodes for the OER and HER with enhanced performance were fabricated for utility confirmation by adjusting the chemical compositions and input electrical parameters. The obtained representative PtNi and Mo-doped non-noble-metal layered double hydroxide (MoNiFe-LDH) catalysts through R2R-FJH suppressed the commercial catalysts with ultralow overpotentials of 31 and 246 mV to achieve 0.5 A cm^{-2} for HER and OER process, respectively. The alkaline water electrolyzer (AWE) cell equipped with the above electrodes offers excellent performance with a cell voltage of 1.66 V to achieve 0.5 A cm^{-2}, along with exceptional stability of over 800 h. To motivate the potential of meter-scale superior electrodes toward hydrogen production, a rolled-up device paradigm was further conceptualized, demonstrating a consistent hydrogen generation with ultrahigh single-cell productivity and near 100% purity. This work provides an attractive solution to the challenges of scalability and homogeneity for industrial water electrolysis.

RESULTS AND DISCUSSION

R2R-FJH to Process Meter-Scale Electrodes. As illustrated in Figure 1a, the R2R-FJH strategy proposed for fabricating meter-scale electrodes is designed to involve three main steps: precursor deposition, flash Joule heating treatment, and rolling-up collection, where flexible conductive nickel foam substrates featuring well-defined porous frameworks and mechanical strength were employed as the R2R conveyors to ensure robust and effective reactions. Theoretically, the cascade synthetic procedures can be outlined as follows: (i) chemical deposition, where precursors are thermochemically nucleated, (ii) in situ growth on substrates through solution evaporation and concentration, and (iii) further thermal stabilization of highly active catalysts. Furthermore, it is noteworthy that the flash Joule heating effect will lead to a more robust interfacial

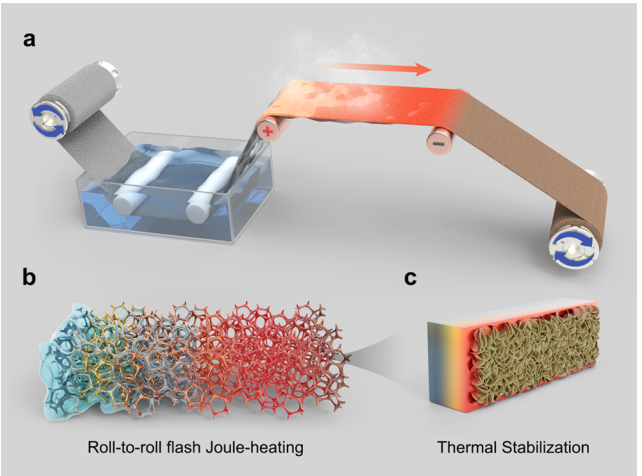

Figure 1. Schematic show of the R2R-FJH strategy. (a) Schematic of the homemade R2R-FJH synthetic system, consisting of precursor deposition, flash Joule heating, and rolled-up collection. (b) Surface precursor deposition and Joule heating effect in the rolling direction. (c) Schematic of thermal stabilization of the catalyst.

binding strength of the designed catalytic nanostructures on the substrate (Figure 1b,c).

To explore the operational dynamics of the R2R-FJH methodology, Figure 2a,b elucidates the working conditions of the designed homemade setup. The establishment of the Joule heating region is achieved through close contact between two cylindrical copper rollers and the conductive conveyor traversing this area, thereby forming a continuous electrical pathway (Figure 2b). The designed substantial resistance difference between the conveyor and copper rollers facilitates the localized heating effect on the specific conveyor to be thermochemically treated when subjected to a direct current (DC) power supply. By experimentally adjusting the speed of the conveyor and input electrical parameters, thermally driven wet-chemical reactions could be continuously conducted under the predetermined temperatures and production rates. In a near-equilibrium state where the conveyor saturated with the precursor solution is heated at both ends of copper rollers, the heating characteristics are completely distinct from the Joule heating effect observed on pure metals.[42,43] For pure metals, Joule heating is driven by the heat generated when current flows through the material, resulting in a typically uniform temperature distribution, which primarily depends on the bulk resistance. In contrast, the presence of the solution plays a critical role in the Joule heating mechanism for the R2R-FJH configuration. The Joule heating generated by the metal substrate can be conducted in situ in the liquid, while the evaporation and concentration of the solution also directly changed the overall macroscopic temperature. It can be observed from the infrared (IR) image of the R2R-FJH region that the dynamic heating characteristic leads to an inhomogeneous distribution in the forward direction of the rolling conveyor (Figure 2c), which are significant for Joule-heating-driven wet-chemical reactions. The surface deposition is accompanied by an elevation of the temperature and the solvent evaporation process, which are closely correlated with the temperature uniformity. The uneven temperature distribution can generate local thermal gradients along with varying local concentration, which can considerably influence the reaction kinetics in specific areas, thereby determining the quality and

https://doi.org/10.1021/acsnano.4c13787
ACS Nano XXXX, XXX, XXX−XXX

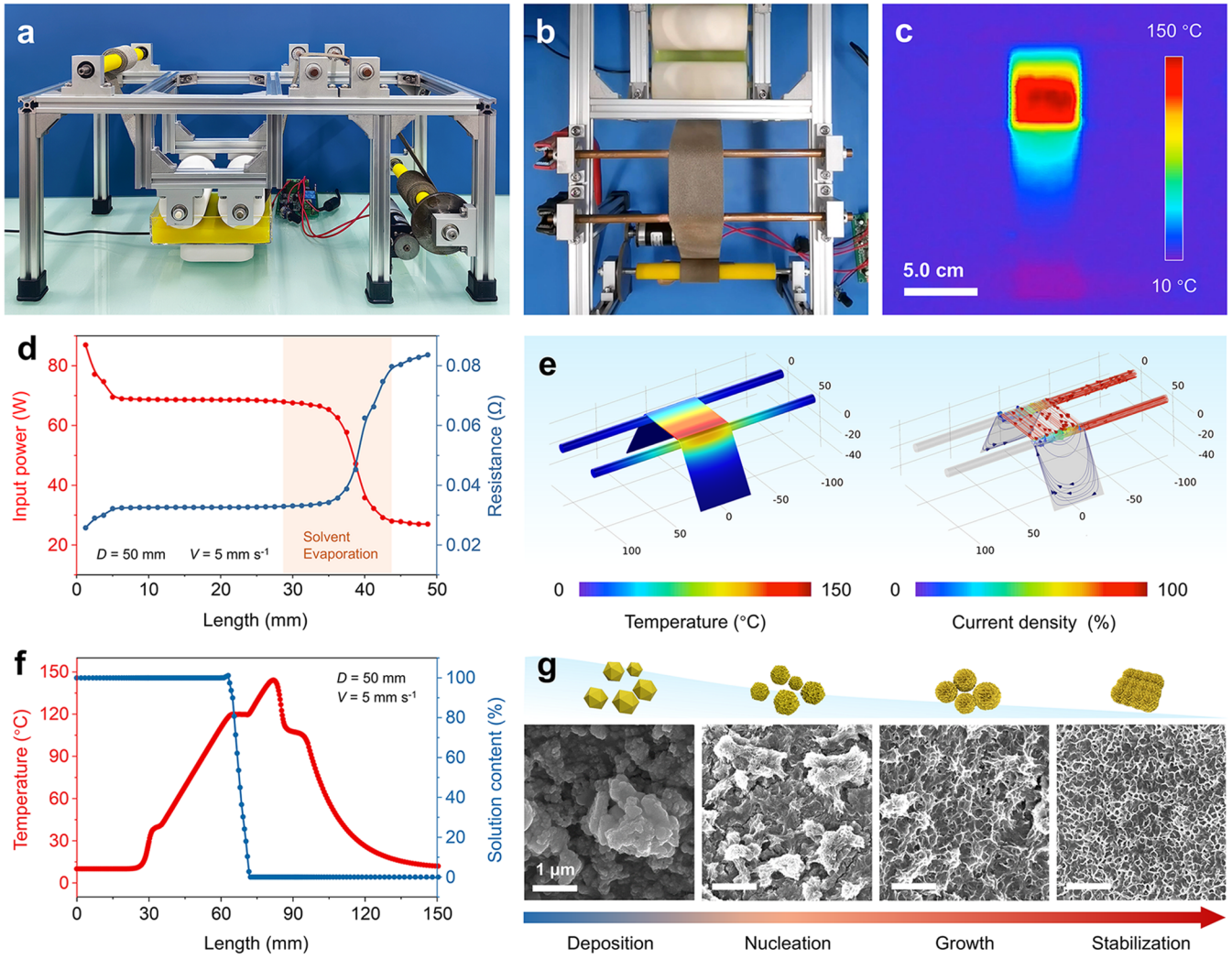

Figure 2. R2R-FJH to process electrode. (a) Optical photograph of the homemade R2R-FJH setup. (b) Localized image of the components of precursor deposition, Joule heating, and product collection. (c) IR image displaying the inhomogeneous temperature distribution of the R2R-FJH region. (d) Profiles of input power and resistance of the conveyor during R2R-FJH. (e) Three-dimensional (3D) simulated images of the temperature and cross-sectional current density distribution of the R2R-FJH region. (f) Simulated profiles of the temperature and solution content varying along the length of the conveyor. (g) Scanning electron microscope (SEM) images and corresponding structural schematics of the designed MoNiFe-LDH, which can be depicted as deposition, nucleation, growth, and thermal stabilization.

uniformity of the deposited materials. With a constant input voltage of 2 V applied to the NF conveyor (D = 50 mm, v = 5 mm s^{-1}), the overall power and body resistance of the electrode tend to stabilize in the presence of the solution, while undergoing dramatic changes as the solvent evaporates (Figure 2d). This can be ascribed to the influence of surface deposits on the electrode, resulting in a marked effect on the thermal conduction properties and overall conductivity.

For an in-depth understanding, computational simulations of the physical field distribution within and surrounding the R2R-FJH region were conducted by COMSOL software (Figure 2e and Supporting Table 1). Under a constant voltage output, the temperature distribution across the electrode surface exhibits a nonuniform distribution, with a rapid decline subsequent to reaching the maximum value at the end of the R2R-FJH region. The difference in thermal distribution between the presence of a solution and pure metal is also well simulated, highlighting the exceptional thermal conductivity at the liquid−solid interface, which provides the dynamics for homogeneous deposition (Figure S1). The concentration of cross-sectional current density reveals that the connected roller and the conveyor collectively constitute the main conductive pathway, validating the precise Joule heating efficiency. Numerical simulation of the surface temperature profile further verifies the temperature-varying behavior of the electrode. As indicated by the simulated profiles, the conveyor is continuously exposed to a relatively dry air-cooling environment, which has specific implications for catalyst growth and stability. Within the R2R-FJH region, the influence of air-cooling through natural convection is minimal, making the temperature remain relatively constant. An overlap is observed between the region of stable temperature and the rapid decrease in solution content, attributed to the continuous evaporation of the boiling solvent (Figure 2f). Following the subsequent heating stage, the temperature of the conveyor undergoes rapid decline due to the excellent thermal conductivity.[44,45] This well-controlled cooling process is also critical for catalyst growth and stabilization. The stable temperature distribution can promote consistent deposition conditions, while the subsequent rapid cooling restrains crystallization and further nucleation to form the desired

https://doi.org/10.1021/acsnano.4c13787
ACS Nano XXXX, XXX, XXX−XXX

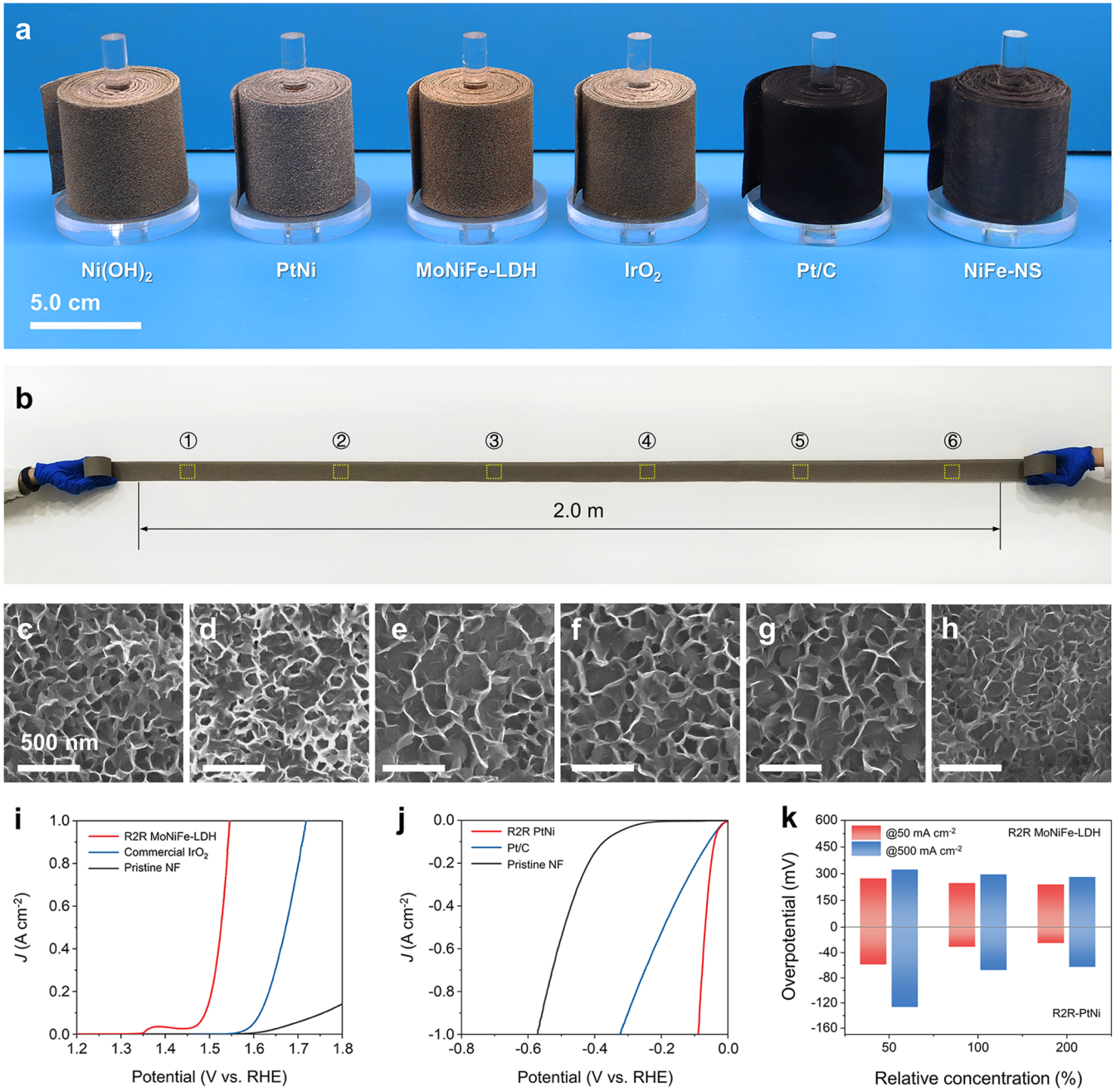

Figure 3. R2R-FJH in meter scale with high uniformity. (a) Various electrodes prepared by R2R-FJH. (b) Various electrodes prepared by R2R-FJH method. Optical photograph of the prepared meter-scale MoNiFe-LDH onto NF electrode. (c–h) SEM images of the randomly selected points on the synthesized MoNiFe-LDH electrode. (i, j) Linear sweep voltammograms (LSV) curves of MoNiFe-LDH and PtNi electrodes compared to commercial catalysts and pristine NF. (k) Overpotential values of electrodes at specific current densities under different relative precursor concentrations.

ultrafine micromorphology. The rapid changes in the thermodynamic state during material growth also contribute to the adhesion of catalytic components onto the substrate, resulting in enhanced structural stability. Moreover, the variations in temperature and surface solution content resulting from diverse widths indicate that optimal electrical parameters enable the programmable regulation of the deposition process, mitigating mechanical breakages and insufficient reactions (Figure S2). Simulation of the heating profiles across various conveyor widths was also conducted, where no nonuniform distribution in the width direction can be observed for any expanded width, validating the potential for further scalability in production (Figure S3).

In a typical synthesis, MoNiFe-LDH integrated on NF was taken as a representative OER catalytic electrode for the R2R-FJH stabilization.[46,47] The working conditions and temperature distribution to produce meter-scale MoNiFe-LDH electrode are demonstrated in Supporting Video 1, showing a reliable, high-throughput, and homogeneous R2R-FJH process. Scanning electron microscope (SEM) images depict the typical ultrathin (oxy)hydroxide nanosheets uniformly growing on the substrate with interconnected networks.[48,49] As displayed in Figure S4, the in-depth morphology and lattice structure were further

https://doi.org/10.1021/acsnano.4c13787
ACS Nano XXXX, XXX, XXX−XXX

characterized by high-resolution transmission electron microscopy (HR-TEM) images, revealing the exposed NiOOH (110) and (101) facets with corresponding lattice fringes of 3.16 and 2.48 Å. Energy-dispersive spectroscopy (EDS) elemental mapping images of MoNiFe-LDH also show a uniform distribution of Ni, Fe, and Mo elements. The fabrication process can be elucidated through sequential SEM images for the synthesis of LDH nanosheets and concluded as a cascade procedure involving deposition, nucleation, growth, and further stabilization (Figure 2g). X-ray diffraction (XRD) was performed to identify the crystalline structures and chemical compositions of the MoNiFe-LDH electrodes. As shown in Figure S5, three diffraction peaks at 44.5, 51.8, and 76.4° can be attributed to the (111), (200), and (220) planes of metallic Ni (PDF No. 87-0712), respectively. Other diffraction peaks with weaker intensity also corresponded well to the typical crystal planes of NiFe-LDH (PDF No. 40-0215) and α-FeOOH (PDF No. 81-0464) for both samples, suggesting the formation of NiFe hydroxide before Mo incorporation. No diffraction peaks corresponding to Mo or its compounds were observed in the XRD pattern of MoNiFe-LDH, indicating that the incorporation of Mo into NiFe-LDH/NF did not result in the formation of a new crystalline phase. To further investigate the contribution of the NF substrate in the hydroxide formation, pristine NF was immersed in ultrapure water and then treated by Joule heating (Figure S6). It can be demonstrated from SEM images and XRD patterns that NiOOH cannot be formed as the only Ni source from the NF substrate within such a short heating duration. The R2R-FJH process relies not only on the thermal effect but also on the rapid nucleation dynamics induced by an excess concentration of precursors. X-ray photoelectron spectroscopy (XPS) was employed to investigate the valence states and electronic structures of the as-prepared MoNiFe-LDH. As shown in Figure S7, the XPS survey spectrum of MoNiFe-LDH demonstrates the presence of elements of Ni, Fe, and Mo, consistent with the results from TEM and XRD. It also confirms that the minimal residual Cl^- or NH_4^+ ions remain after the R2R-FJH process, ensuring no adverse impact on electrode performance. Based on the peak table, the atomic ratio of Ni to Fe is approximately 4:1, with Mo element accounting for 0.84 wt %. The Mo 3d spectrum of MoNiFe-LDH (Figure S8a) clearly displays two peaks at 232.1 and 235.2 eV, which can be attributed to Mo^{6+} $3d_{5/2}$ and Mo^{6+} $3d_{3/2}$, respectively.[50] The Ni 2p XPS spectrum of MoNiFe-LDH in Figure S8b can be split into $2p_{3/2}$ and $2p_{1/2}$ due to spin−orbit coupling, with characteristic peaks located at 855.5 and 873.2 eV corresponding to Ni^{2+}, and additional peaks at approximately 861.5 and 879.7 eV identified as satellite peaks. Additionally, Ni^{3+} species are identified at 857.1 and 875.3 eV, suggesting the formation of NiOOH with enhanced conductivity in the MoNiFe-LDH structure.[51] For the Fe 2p XPS spectrum in Figure S8c, aside from the two satellite peaks, the peaks at 708.9 and 722.8 eV are attributed to Fe^{2+}, while those at 713.8 and 726.7 eV are assigned to Fe^{3+}. As shown in Figure S8d, the O 1s XPS spectrum exhibits characteristic peaks at 531.7, 533.5, and 535.4 eV, corresponding to lattice oxygen, oxygen vacancies, and hydroxyl groups, respectively. This result indicates that Mo doping modifies the intrinsic electronic structure of the NiFe-LDH, leading to an increase in the concentration of oxygen vacancies.

Differing from the traditional solvothermal and corrosive synthesis, this R2R-FJH route enables the rapid establishment of the required thermochemical conditions characterized by high concentration and substeady temperature distribution.[52] The contact angle (CA_{water}) of MoNiFe-LDH is measured as 9.4°, significantly lower than 112.8° of the pristine NF, indicating the superhydrophilicity derived from the surface chemical deposition, which can accelerate the desorption of bubbles and prevent the polarization (Figure S9).[53] To expand the application of the strategy in the field of electrolytic water splitting, ultrafine Pt clusters on nickel oxide supports as an advanced catalytic electrode (PtNi) for HER were also synthesized by the R2R-FJH method using H_2PtCl_6 as the precursor. HRTEM images reveal that Pt nanoclusters possess sizes of approximately 1−2 nm and are uniformly distributed on partially crystalline nickel oxide carriers. The homogeneous distribution of elements shown in the EDS mapping images also confirms the notable enhancement of the Joule heating strategy on the dispersion of metallic species (Figure S10). The total loading amount of Pt in the PtNi electrode was identified as 0.607 mg cm^{-2} by inductively coupled plasma optical emission (ICP-OES).

To further validate the universality of the R2R-FJH strategy for different precursors and substrates, diverse types of catalysts stabilized onto meter-scale electrodes were successfully prepared for demonstration with a width of 50 mm, which satisfies the majority of laboratory cell performance evaluations (Figure 3a). Additionally, commercial IrO_2 and Pt/C catalysts could be uniformly deposited onto NF electrodes through direct solvent evaporation and thermal stabilization. The typical SEM images of these electrodes are presented in Figure S11, showcasing the desired morphologies by design of precursors and operational parameters. A typical meter-scale MoNiFe-LDH electrode using NF substrate is displayed in Figure 3b, emphasizing the substantial potential of the R2R-FJH strategy to meet the demands of practical industrial large-scale processing. Upon several points on a randomly selected section of the synthesized conveyor electrode, the microstructures exhibit minimal variations (Figure 3c−h). The electrocatalytic OER performances (Figure S12) and key comparative electrochemical data (Supporting Table 2) tested in these areas are nearly identical, underscoring the impressive advantage of the R2R-FJH method on homogeneity. This approach offers significant prospects for enhancing the production, uniformity, and scalability of industrial electrolyzers. The ability to fabricate large-area electrodes with consistent microstructural characteristics facilitates the integration of electrodes into commercial systems, ensuring reliable performance across extensive operational conditions. Furthermore, continuous processing can lead to increased production rates, which are crucial for meeting the rising demand for advanced electrode components.

Electrochemical Performance. The electrochemical performance of the fabricated electrodes was measured in 1 M KOH (pH = 14) by using a typical three-electrode configuration at room temperature. Figure 3i illustrates the linear sweep voltammograms (LSV) curves of different samples toward the OER. The MoNiFe-LDH electrode through R2R-FJH demonstrates extraordinary OER activity with ultralow overpotentials of 246 and 295 mV to achieve 50 and 500 mA cm^{-2} (η_{50} and η_{500}), accompanied by the lowest Tafel slope of 52.2 mV dec^{-1}, indicating the fastest reaction kinetics. This result exceeds the performance of commercial IrO_2 and NF electrodes evaluated under the same condition. The exceptional activity can be attributed to its unique layered structure, while appropriate Mo doping promotes efficient charge transport and the availability of active sites, leading to intrinsic catalytic activity surpassing that of IrO_2.[54−56] As shown in Figure 3j, the PtNi catalyst onto NF substrate also exhibits the competitive η_{50} and η_{500} of 31 and 68

https://doi.org/10.1021/acsnano.4c13787
ACS Nano XXXX, XXX, XXX−XXX

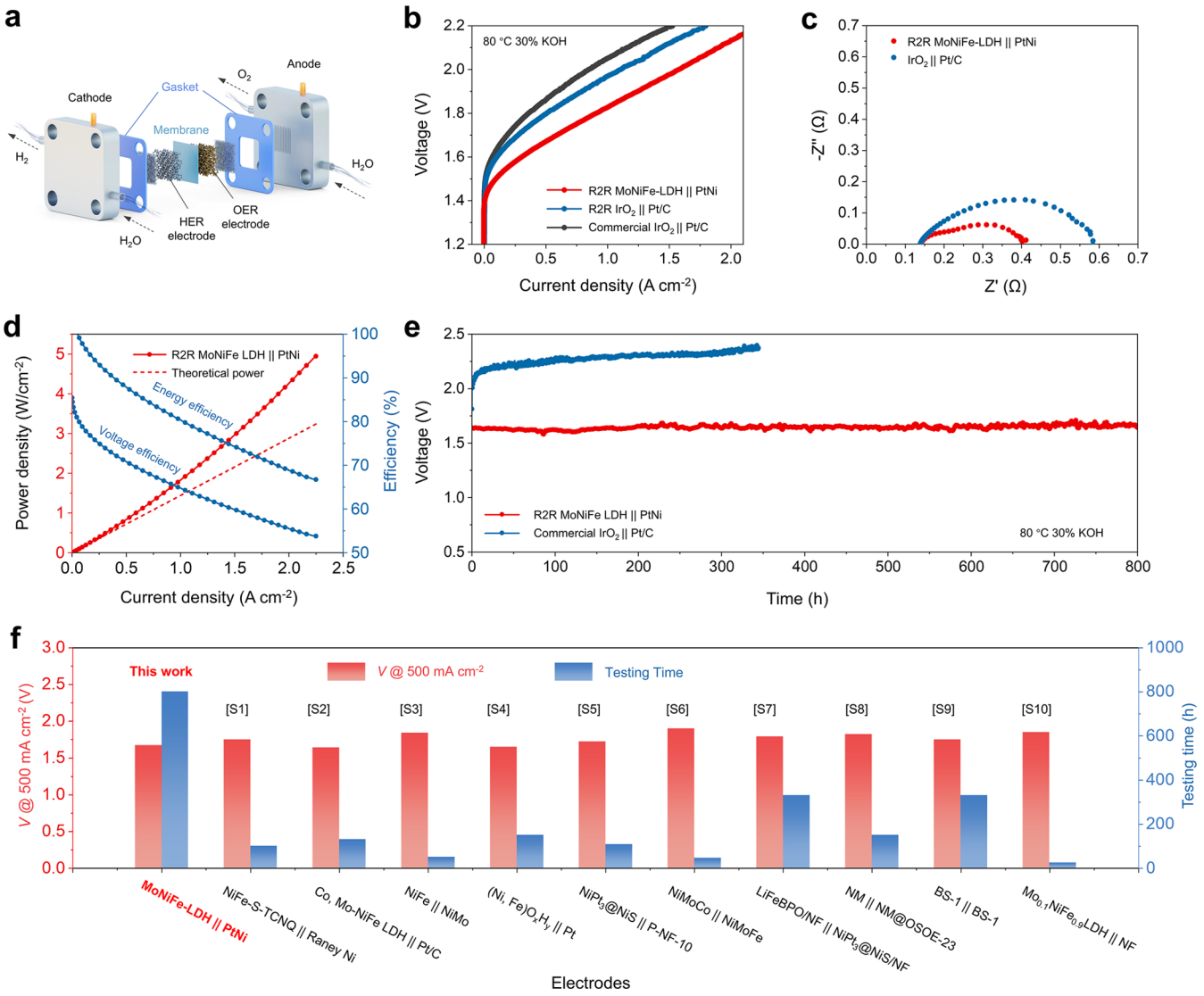

Figure 4. Electrocatalytic performance in AWE cell. (a) Structural schematic of the AWE cell. (b) Polarization curves of the R2R MoNiFe-LDH || PtNi compared to IrO_2 || Pt/C through R2R-FJH and spray-coating. (c) Nyquist impedance plots of the AWE cells under 0.5 A cm^{-2}. (d) Power density, energy efficiency, and voltage efficiency as a function of the current density for MoNiFe-LDH || PtNi. (e) Durability cell voltage−time curve at 0.5 A cm^{-2} of MoNiFe-LDH || PtNi compared to spray-coated IrO_2 || Pt/C. (f) Comparison with other reported works in the cell voltage to achieve 0.5 A cm^{-2} and testing time.

mV higher than that of commercial Pt/C and pristine NF, respectively, along with the exceptional Tafel slope of 29.4 mV dec^{-1}. To further elucidate the growth and stabilization process during R2R-FJH, the electrochemical performance of MoNiFe-LDH and PtNi samples obtained from different positions at the heating region (denoted as sample-*x*, *x* = 1, 2, and 3 in Figure S13) were evaluated. As depicted in Figures S14 and S15, the electrodes in the heating zone exhibited progressively improved catalytic activities from the rolled-in part to the end during the R2R-FJH procedure, indicating the increasing contents of electrochemically active substances, which also corresponds to the results in Figure 2h. The Nyquist plots for both MoNiFe-LDH and PtNi electrodes through R2R-FJH exhibit the smallest R_{ct} values among various comparative samples, revealing the enhanced charge transfer kinetics of the electrochemical process (Figure S16).

To reveal the catalytic performance, the electrochemically active surface area (ECSA) for electrodes was calculated based on the double-layer capacitance (C_{dl}) calculated by cyclic voltammetry (CV) measurements performed at different scan rates of 10−50 mV s^{-1} in the non-Faradaic potential window (Figures S17 and S18). As shown in Figure S19, the C_{dl} values for MoNiFe-LDH-3 (49.9 mF cm^{-2}) and PtNi-3 (52.4 mF cm^{-2}) illustrated from the fitting line were significantly higher than those of comparative electrodes, indicating larger ECSA values and more active sites exposure. The normalized current density (j_{ECSA}) calculated by ECSA values from different parts of the conveyor is displayed in Figure S20 and Supporting Table 3, demonstrating the highest intrinsic catalytic activity of the MoNiFe-LDH-3 and PtNi-3 samples through R2R-FJH. The impact of precursor concentration on electrode performance was also evaluated (Figure 3k). An appropriate precursor concentration (denoted as 100%) can provide the optimal density and distribution of active sites, leading to excellent catalytic performance. The significant decrease in overpotential at 50% of the initial concentration generally leads to the insufficient formation of active sites, while at 200%, although the performance improves slightly, the higher concentration can still

https://doi.org/10.1021/acsnano.4c13787
ACS Nano XXXX, XXX, XXX−XXX

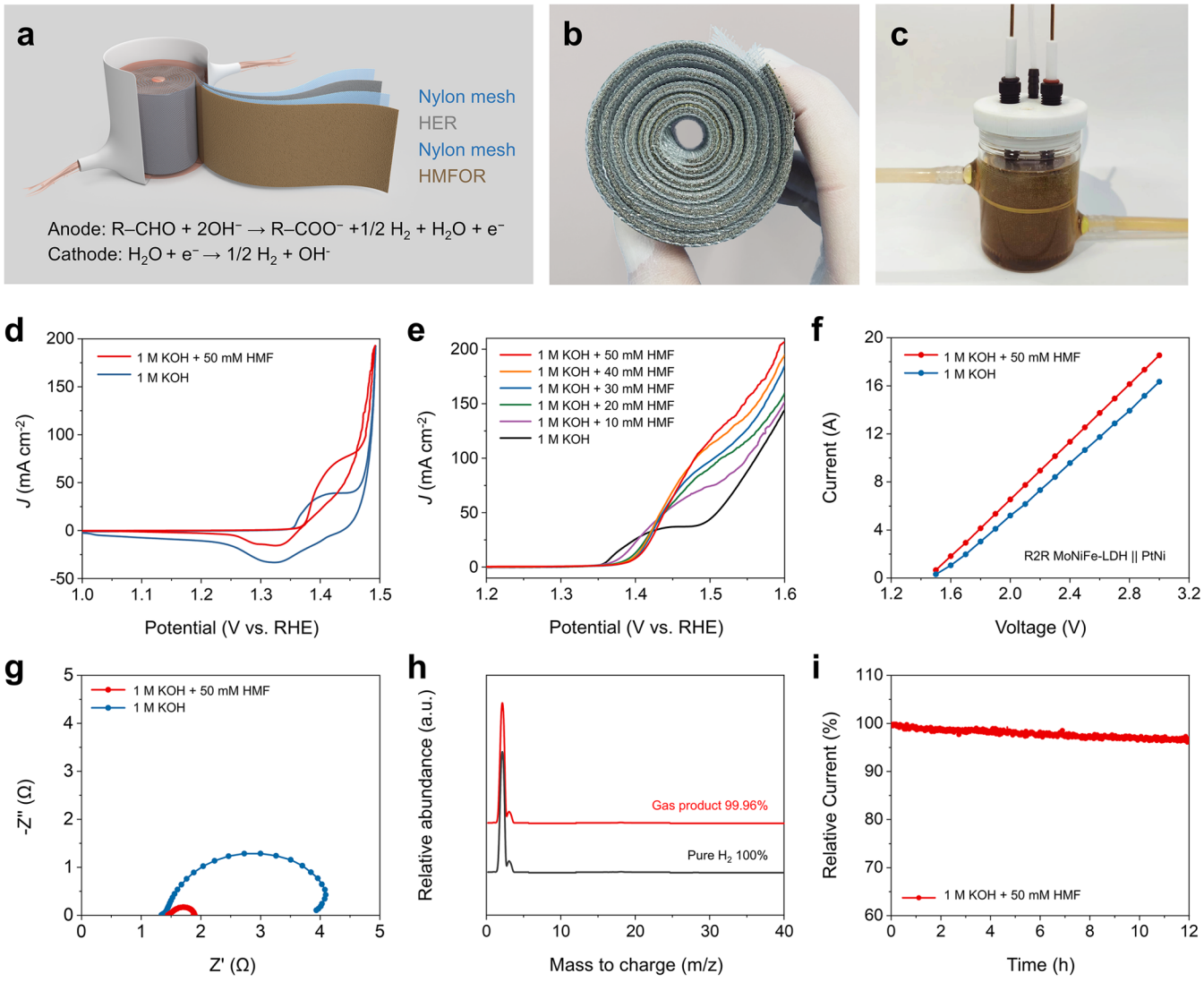

Figure 5. Rolled-up electrodes for hydrogen production. (a) Schematic illustration and reaction mechanism of the system. (b) Optical photographs of the rolled-up assemblies. (c) The corresponding hydrogen production device. (d) CV curves of the MoNiFe-LDH electrode with and without 50 mM HMF in 1 M KOH. (e) LSV curves of the MoNiFe-LDH electrode with various HMF concentrations in 1 M KOH. (f) Current profiles as a function of input voltage and (g) Nyquist impedance plots of the rolled-up prototype with and without 50 mM HMF. (h) Mass spectrometry (MS) results for the collected and pure hydrogen samples. (i) CA test of the hydrogen production system at a constant current of 10 A.

lead to excessive aggregation of the precursor, which may negatively impact the homogeneous surface structure.[57] To further evaluate the effectiveness of the R2R-FJH process, electrocatalytic performance for the MoNiFe-LDH catalysts under various optimized conditions is also provided. As illustrated in the LSV curves in Figure S21, an appropriate combination of conveyor speed and heating power enables the optimized nucleation and growth of the precursors onto the NF substrate. This optimization ensures the maximum active site density while effectively preventing performance degradation caused by overheating or an incomplete reaction. Moreover, long-term durability is another essential criterion for evaluating the performance of the catalytic electrodes. The durability of the samples was initially evaluated by the accelerated durability test (ADT) using consecutive CV cycles. Both the LSV curves of MoNiFe-LDH and PtNi almost overlapped the initial curves even after 50,000 CV cycles (Figure S22). The above electrodes also exhibit negligible degradations after chronoamperometry (CA) for 24 h, indicating overwhelming superiority to commercial IrO_2 and Pt/C catalysts (Figure S23). The MoNiFe-LDH and PtNi electrodes with enhanced structural robustness still maintained their pristine structures and morphologies after long-term stability test. In contrast, the degradation observed in IrO_2 and Pt/C is primarily attributed to the weak bonding strength onto the substrate, which can lead to dissolution or agglomeration under harsh operating conditions at higher current densities (Figures S24 and S25). Furthermore, the binding stability of catalysts onto the substrate was verified by ultrasonication in water for 10 min (Figure S26). Almost no exfoliation of active substances can be observed after ultrasonication of the MoNiFe-LDH electrode prepared by R2R-FJH. SEM images taken before and after ultrasonication with almost no morphological changes and detachment also demonstrated the strong bonding of catalyst onto the substrate resulting from Joule heating process (Figure S27). In contrast, the solution where the NiFe-LDH sample prepared by

https://doi.org/10.1021/acsnano.4c13787
ACS Nano XXXX, XXX, XXX−XXX

electroplating irradiated with a laser pointer showed a visible Tyndall effect attributed to the presence of massive solute, while most catalysts deposited onto the substrate were detached (Figure S28).

Considering the outstanding performance of three-electrode system, a single zero-gap AWE cell was further constructed to investigate the overall water splitting performance under practical working conditions, using circulated KOH electrolyte with a stable 30% concentration at 80 °C in Figures 4a and S29.[58−61] The polarization curves without *iR* correction of the electrolyzer using MoNiFe-LDH and PtNi electrodes are shown in Figure 4b, exhibiting outstanding electrolytic performance with the cell voltage of only 1.66 and 1.82 V to reach 0.5 and 1.0 A cm^{-2}, much better than the comparative cells constructed by commercial IrO_2 || Pt/C. It is worth noting that the AWE cell using commercial electrodes prepared through R2R-FJH exhibits a lower cell voltage compared to those prepared by spray-coating. This improvement can be attributed to the thermal effects of R2R-FJH, which facilitates the bonding strength between the catalyst layer and substrates, thereby improving the structural stability of the device. Additionally, the R2R-FJH method ensures more homogeneous catalyst deposition, which increases the utilization of active sites and improves the overall catalytic performance. Characterized by Nyquist impedance plots, the charge transfer resistance of MoNiFe-LDH || PtNi is significantly lower than that of commercial one, which can be attributed to the higher intrinsic activity and rapid charge transfer kinetics of the electrodes (Figure 4c). The evaluated cell voltage values at 0.5 and 1.0 A cm^{-2} correspond to the energy efficiencies of 87.5 and 80.4% (calculated by the higher heating value of H_2), respectively, with the voltage efficiencies of 70.8 and 64.7% (Figure 4d).[62] As shown in Figure S30, a more comprehensive comparison with the state-of-the-art NiFe-LDH electrode was conducted to highlight the advantages of the MoNiFe-LDH catalyst in alkaline electrolyte. The MoNiFe-LDH sample exhibits significantly improved catalytic activity and charge transfer efficiency in both three-electrode system and the AWE cell, demonstrating that Mo doping is essential for optimizing the electronic structure of NiFe-LDH and enhancing its intrinsic catalytic activity. Furthermore, the stability of the electrolyzers was measured by chronopotentiometry (CP) test. The MoNiFe-LDH || PtNi cell exhibited excellent durability with a stable cell voltage at 0.5 A cm^{-2} for 800 h and a degradation rate ≈75 $\mu V\ h^{-1}$, which is much lower than commercial IrO_2 || Pt/C (Figure 4e). The outstanding performance and long-term stability of single AWE cells further confirm the potential of electrodes prepared through the R2R-FJH strategy for application on mainstream electrolysis devices for advanced water splitting (Figure 4f and Supporting Table 4).

Rolled-Up Prototype for Hydrogen Production. Motivated by the widely utilized coiled cell structure in the field of LIBs, a novel rolled-up two-electrode configuration has been developed for practical hydrogen production.[63,64] This configuration capitalizes on the unique advantages of the R2R-FJH strategy, which allows for the maximal use of the continuous meter-scale electrodes fabrication. By integration of these electrodes into the rolled-up system, the configuration enhances structural integrity and reaction kinetics, thereby facilitating large-scale hydrogen evolution at low cell voltages in a single-cell setup. Due to the membrane-free design, separation of hydrogen and oxygen became the prime challenge to be solved for the system. As an attractive strategy to reduce the cost of electrocatalytic hydrogen production, replacing the anodic OER with a more efficient biomass electrooxidation reaction can eliminate oxygen generation and reduce the cell voltage, while generating high-value chemicals. For example, 5-hydroxymethylfurfural oxidation reaction (HMFOR) in alkaline media exhibits better kinetic properties and a lower theoretical potential compared to the OER, with the typical product 2,5-furandicarboxylic acid (FDCA) as an important monomer to produce biobased polymers. In this process, adsorbed HMF* intermediates are formed by the incorporation of HMF molecules onto the catalyst, which are then oxidized by the absorbed hydroxyl groups (OH_{ads}). Subsequently, the hydroxyl and aldehyde groups of HMF are oxidized to generate the corresponding oxidation products and H_2O.[65,66] The circulating liquid flow was incorporated to maintain a constant electrolyte concentration, providing a stable electrochemical state during the long-term HMFOR process (Figure 5a).[67] Within the coiled two-electrode structure, Nylon mesh was used to separate the cathodic and anodic components, facilitating gas transfer and subsequent collection in conjunction with three-dimensional networks of NF (Figure 5a,b).

The optical photograph of a rolled-up hydrogen-producing cell is depicted in Figure 5c, utilizing MoNiFe-LDH and PtNi through R2R-FJH as the cathode and anode, respectively. The total area of electrodes is 1000 cm^2, and sealed components were required to ensure gas tightness (Figures 5c and S31). In the presence of 50 mM HMF, the CV curve of the MoNiFe-LDH electrode is significantly different from that in 1 M KOH with the appearance of a higher characteristic peak corresponding to the redox reaction of the Ni^{2+}/Ni^{3+}, indicating the excellent reactivity toward HMFOR (Figure 5d). As the concentration of HMF gradually increased from 10 to 50 mM, the current density of the MoNiFe-LDH electrode at higher potentials was also increased, suggesting an increase in the current contribution to the HMFOR process (Figure 5e). In the two-electrode tests, stable operation of the rolled-up device under the current of several amperes is achieved with an input voltage comparable to that of typical AWE devices.

The larger electrode area facilitates the entire system to maintain a lower current density, effectively avoiding detachment and mass transfer issues. The presence of 50 mM HMF significantly increases the current values, further demonstrating the excellent selectivity toward HMFOR (Figure 5f). Nyquist plots of the MoNiFe-LDH || PtNi assemblies with the participation of 50 mM HMF further confirmed faster charge transfer and higher catalytic activity (Figure 5g). As displayed in Figure 5h, the purity of the generated hydrogen from the rolled-up system was determined by mass spectrometry (MS), which exhibited an excellent purity of 99.96% close to that of standard pure hydrogen, confirming the applicability of the setup for practical hydrogen production under the coupling of HMFOR and HER. The CA curve tested at an initial current of 10 A exhibits only a slight decay, further illustrating the long-term stability of the rolled-up configuration, which is attributed to the robustness of electrodes and the entire system and exhibits great potential for membrane-free electrochemical water splitting (Figure 5i). These results not only highlight the operational efficiency of the rolled-up configuration but also underscore its potential to revolutionize hydrogen production methods. The scalability and robustness demonstrated by this system suggest its potential for further optimization and integration into commercial electrolyzers, thereby contributing to the advancement of sustainable energy technologies.

https://doi.org/10.1021/acsnano.4c13787
ACS Nano XXXX, XXX, XXX−XXX

CONCLUSIONS

The R2R-RJH methodology presents a promising solution to address the challenges of scalability and uniformity in the production of advanced electrodes for industrial water electrolysis while maintaining both exceptional catalytic activity and stability. Its salient attributes encompass a serial coupling of nonproblematic thermal nucleation, steady-state chemical growth, and further stabilization of catalysts onto substrates by R2R processing. Our advancement of the R2R-RJH strategy further underscores its superior versatility and scalability by the instant and precise electrical control, which enables rapid meter-scale electrode patterning and modification. The fascinating performance of R2R-RJH stabilized electrodes has been rigorously validated in three-electrode system and typical AWE cell testing, far outperforming commercial IrO_2 and Pt/C electrodes. Furthermore, a novel rolled-up and membrane-free configuration using coiled electrodes has been developed, showcasing the continuous production of high-purity hydrogen combined with an anodic HMFOR substitution. Considering the rapid surface deposition and modulation dynamics under R2R manner, ensured by the steady but inhomogeneous thermal condition, the R2R-FJH route not only provides a distinctive approach to scalable processing and efficient application mode for high-quality electrodes in advanced water splitting but also offers substantial potential for a wide range of industrial thermochemical synthesis and applications.

EXPERIMENTAL SECTION

Materials. Nickel chloride hexahydrate ($NiCl_2{\cdot}6H_2O$, Aladdin, >98%), ferric chloride hexahydrate ($FeCl_3{\cdot}6H_2O$, Aladdin), $(NH_4)_6Mo_7O_{24}{\cdot}4H_2O$ (Sinopharm Chemical Reagent Co., Ltd.), chloroplatinic acid ($H_2PtCl_6{\cdot}6H_2O$, AR, Pt ≥ 37.5%, Aladdin), potassium hydroxide (KOH, 99 wt %), commercial IrO_2 (Sigma-Aldrich, 99.9%), commercial Pt/C (20 wt % Pt on Vulcan XC-72R, JM), absolute ethanol (C_2H_5OH, 99.8%, Aladdin), 5-hydroxymethylfurfural (HMF, 98%, Sigma-Aldrich), nickel foam (1 mm thick, 110 ppi, Lizhiyuan Co. Ltd.), nickel mesh (NM, obtained from Kunshan Baiyida Electronic New Material Company, China), carbon felt (CF, obtained from Kunshan Baiyida Electronic New Material Company, China), deionized water (18 $M\Omega{\cdot}cm^{-1}$), hydrochloric acid (HCl, 37%, Sinopharm Chemical Reagent Co., Ltd.), and ultrathin carbon film on holey carbon (400 mesh, copper gird, Ted Pella, Inc.). All of the chemicals were used without further purification.

Construction of the R2R-FJH Setup. The homemade R2R-FJH system was constructed by aluminum extrusion profiles, shafts, bearings, and other components. Stainless steel rollers with a polyurethane coating were utilized in the loading and collecting section of conveyors. Rollers made of Teflon were applied where the conveyor was partially immersed in the precursor solutions to ensure good liquid impregnation. A magnetic stirrer was set up underneath the vessel containing the precursor solution to ensure homogeneity. In the Joule heating thermal treatment, two rollers made of purified copper with a diameter of 8 mm and a spacing of 50 mm were acting as the positive and negative terminals connected to the DC power supply (IT6512 C, ITECH Electronic Co., Ltd., China) by means of clamping at both ends. At the part for conveyor collection, a 12 V DC motor and a speed controller were employed to regulate the speed of the whole system. The overall system was carefully verified for coaxially and smoothness to ensure a reliable R2R process, and insulated ceramic bearings were utilized at all electrical conduction sites to ensure the established current pathway.

Preparation of the MoNiFe-LDH Electrode. The MoNiFe-LDH electrode was synthesized by the R2R-FJH method proposed in this work. Typically, a nickel foam conveyor (length = 2 m, width = 5 cm) was cut and ultrasonically cleaned in a 3 M HCl solution to remove the surface oxide layer and impurities. The conveyor was subsequently washed with deionized water and ethanol, and then dried in 50 °C vacuum under the pressure of −0.1 MPa. 6.75 g of $FeCl_3{\cdot}6H_2O$, 3.25 g of $NiCl_2{\cdot}6H_2O$, and 670 mg of $(NH_4)_6Mo_7O_{24}{\cdot}4H_2O$ were dissolved in 300 mL of DI water and dispersed with sufficient sonication to serve as the precursor solution. During the proceeding R2R synthesis, the input voltage of the DC power supply was kept at 2.5 V, and the total input power was about 75−80 W. The slight power variations were attributed to the minor structural differences among the commercial NF materials. The conveyor was moved at a constant speed of 5 mm s^{-1} until it was completely collected. The desired meter-scale MoNiFe-LDH electrode was finally obtained by washing the obtained conveyor with DI water.

Preparation of the PtNi Electrode. The PtNi electrode was synthesized by the R2R-FJH method proposed in this work. Typically, a nickel foam conveyor (length = 2 m, width = 5 cm) was cut and ultrasonically cleaned in a 3 M HCl solution to remove the surface oxide layer and impurities. The conveyor was subsequently washed with deionized water and ethanol, and then dried in 50 °C vacuum under the pressure of −0.1 MPa. 0.4 g $H_2PtCl_6{\cdot}6H_2O$ powder was dissolved in 300 mL of DI water and dispersed with sufficient stirring to serve as the precursor solution. During the proceeding R2R-FJH synthesis, the input voltage of the DC power supply was kept at 2.8 V and the total input power was about 95−100 W. The conveyor was moved at a constant speed of 5 mm s^{-1} until it was completely collected. The desired meter-scale PtNi electrode was finally obtained by washing the obtained conveyor with DI water.

Preparation of the $Ni(OH)_2$ Electrode. The $Ni(OH)_2$ electrode was synthesized by the R2R-FJH method proposed in this work. Typically, a nickel foam conveyor (length = 2 m, width = 5 cm) was cut and ultrasonically cleaned in a 3 M HCl solution to remove the surface oxide layer and impurities. The conveyor was subsequently washed with deionized water and ethanol and then dried in 50 °C vacuum under the pressure of −0.1 MPa. 300 mL of 6 M KOH was prepared to serve as the precursor solution. During the proceeding R2R synthesis, the input voltage of the DC power supply was kept at 2.5 V and the total input power was about 75−80 W. The conveyor was moved at a constant speed of 5 mm s^{-1} until it was completely collected. The desired meter-scale $Ni(OH)_2$ electrode was finally obtained by washing the obtained conveyor with DI water.

Preparation of the Commercial IrO_2 and Pt/C Electrodes. The commercial IrO_2 and Pt/C electrode was synthesized by the CJH method (physical deposition) proposed in this work. Typically, a nickel foam conveyor (length = 2 m, width = 5 cm) was cut and ultrasonically cleaned in a 3 M HCl solution to remove the surface oxide layer and impurities. The conveyor was subsequently washed with deionized water and ethanol, and then dried in 50 °C vacuum under the pressure of −0.1 MPa. 4.80 g of commercial IrO_2 or 3.75 g of commercial Pt/C was dissolved in 300 mL of DI water and dispersed with sufficient sonication to serve as the precursor solution, respectively. During the proceeding R2R-FJH synthesis, the input voltage of the DC power supply was kept at 2.5 V, and the total input power was about 75−80 W. The conveyor was moved at a constant speed of 5 mm s^{-1} until the desired electrode was completely collected.

Preparation of Other Meter-Scale Electrodes. Other meter-scale electrodes with different widths were synthesized by the R2R-FJH method proposed in this work. After the infiltration of the designed precursor solution, the conveyors were continuously heated under the DC power supply. The input power can be programmatically adjusted over time to allow for the rapid thermochemical growth and stabilization of surface deposits. Meanwhile, rational power setups, which are related to conveyor width, speed, and reaction temperature, contribute to the prevention of overheating and breakage. The desired meter-scale electrodes were finally obtained by collecting and washing the produced conveyors.

Materials Characterizations. The morphology of the prepared electrodes and catalysts was characterized by high-angle annular dark-field scanning transmission electron microscopy (HAADF-STEM) and high-resolution transmission electron microscopy (HRTEM) images acquired on a 2100F transmission electron microscope operated at 200 kV and scanning transmission electron microscopy (FE-SEM, S-4800, Japan) equipped with energy dispersion spectra (EDS) and elemental

https://doi.org/10.1021/acsnano.4c13787
ACS Nano XXXX, XXX, XXX−XXX

mapping. XRD characterization of the samples was performed at room temperature using a *D*/max 2500 V X-ray diffractometer equipped with Cu Kα radiation, operated at approximately 40 kV and 150 mA, with a scan rate of 8° min^{-1}. XPS measurements were obtained by using an X-ray photoelectron spectrometer (Escalab 250Xi) equipped with an Al Kα radiation source (1487.6 eV) and a hemispherical analyzer with a pass energy of 30.0 eV and an energy step size of 0.05 eV. The binding energy of the C 1s peak at 284.8 eV was considered as an internal reference. Spectral deconvolution was applied by Shirley background subtraction using a Voigt function convoluting the Gaussian and Lorentzian functions. The total noble-metal loading contents on substrates were identified by inductively coupled plasma-mass spectrometry (ICP-MS, ELAN DRC-e) measurements. The surface temperature of the samples was visualized using an infrared (IR) thermal imager (CEM DT-980, Huashengchang Co., Ltd., China).

Electrochemical Measurement. The single-electrode electrochemical tests for the OER and HER were performed using a typical three-electrode electrochemical cell using an Autolab potentiostat (PGSTAT-204N) equipped with Nova 1.11 software in 1 M KOH electrolyte. An as-prepared catalytic electrode, a graphite rod, and a Hg/HgO electrode were involved as the working electrode, counter electrode, and reference electrode, respectively. The geometry of the single electrode testing is 1.0 cm^2 for both OER and HER processes. All polarization curves were collected at a scan rate of 5 mV s^{-1} and calibrated to the reversible hydrogen electrode according to the following equation: $E_{RHE} = E_{Hg/HgO} + 0.098 + 0.059 \times pH$. The Tafel plots were constructed using the current density obtained from the LSV curves through the Tafel equation: $\eta = a + b \log (j)$, where η is the overpotential, j is the current density, a is the intercept of the Tafel plot, and b is the Tafel slope. The *iR* compensation level of 90% based on the electrochemical impedance spectroscopy (EIS) analysis was applied and performed between a frequency ranging from 100 kHz to 0.1 Hz with a potential amplitude of 50 mV. The specific potential values used in linear sweep voltammetry (LSV) measurements are 0.2−1.0 and −0.9 to −1.9 V for the OER and HER tests, respectively. The long-term stability test was evaluated by chronoamperometry (CA) measurements at an initial current density of 100 mA cm^{-2} for 24 h along with accelerated durability test (ADT) using cyclic voltammetry (CV) cycles at a scan rate of 100 mV s^{-1} for 10,000 and 50,000 cycles. The specific potentials applied in ADT tests are 0.2−0.6 and −0.9 to −1.1 V for the OER and HER tests, respectively. Each electrochemical CV and LSV test was conducted in N_2-saturated 1 M KOH to minimize the influence of impurity gases, ensuring accurate and reliable measurements. Each electrochemical test was repeated more than three times to ensure reproducibility, continuing until consistent results were obtained. The normalized current density (j_{ECSA}) from different parts of the conveyor can be performed using the formula

$$j_{ECSA} = i/\mathrm{ECSA}$$

$$\mathrm{ECSA} = C_{dl}/C_s \times A$$

where i represents the current from the LSV curves, C_{dl} is the double-layer capacitance, C_s is a specific capacitance constant of an identical flat surface (40 $\mu F/cm^2$ for 1 M KOH in this work), and A is the geometric area of electrode.

The two-electrode hydrogen production (anode: HMFOR and cathode: HER) was executed in a single cell with circulating electrolyte flow using the proposed rolled-up configuration consisting of meter-scale MoNiFe-LDH-NF, PtNi-NF, and Nylon mesh. The LSV and CV curves in different concentrations of HMF in 1 M KOH ranging from 0 to 50 mM were evaluated at room temperature. EIS analysis was applied and performed between a frequency ranging from 100 kHz to 0.1 Hz with a potential amplitude of 50 mV under the total current value of 5.0 A. The long-term stability test was evaluated by CA measurements at an initial current of 10.0 A for 24 h. The H_2 gas purity was identified by PM-QMS online gas mass spectrometry (Shanghai Pro-tech Co., Ltd., China) and calculated by comparing the relative abundance values.

Finite Element (FE) Simulation Method. The finite element (FE) simulations of the temperature and current distributions taking the NF conveyor as an example were performed by using COMSOL Multiphysics 6.2 software. Three-dimensional geometric models were established based on the dimensions of the electrical rollers and electrode sheets in the experiments. After adjustment of the model, the geometry is assigned the relevant material properties and meshed. Subsequently, mutually coupled multiphysics fields were set up for the models, and the results were then visualized. Specifically, one copper electrode was used for input voltage, and the other was grounded. The electrode conveyor impregnated with the precursor solution is driven forward by the rollers with a certain speed. Electric current flows through a copper roller, a rolling belt thin sheet, and another copper roller. During this process, the generated Joule heating heats the electrode thin conveyor, leading to evaporation of the surface solvent.

ASSOCIATED CONTENT

Supporting Information

The Supporting Information is available free of charge at https://pubs.acs.org/doi/10.1021/acsnano.4c13787.

Simulated images and profiles, SEM and TEM images, XRD patterns, XPS spectra, elemental mapping results, photographs of contact angles, electrochemical performance, and optical photographs of the AWE cell and the rolled-up hydrogen production system (Figures S1−S24) (Tables S1 and S2) (PDF)

Operation and temperature distribution of the R2R-FJH setup (Video 1) (MP4)

AUTHOR INFORMATION

Corresponding Authors

Kai Huang − *School of Science, Beijing University of Posts and Telecommunications, Beijing 100876, China;* orcid.org/0000-0002-1820-6221; Email: Huang-kai@bupt.edu.cn

Hui Wu − *State Key Laboratory of New Ceramics and Fine Processing, School of Materials Science and Engineering, Tsinghua University, Beijing 100084, China;* orcid.org/0000-0002-4284-5541; Email: huiwu@tsinghua.edu.cn

Authors

Peng Du − *School of Science, Beijing University of Posts and Telecommunications, Beijing 100876, China; State Key Laboratory of New Ceramics and Fine Processing, School of Materials Science and Engineering, Tsinghua University, Beijing 100084, China*

Bohan Deng − *State Key Laboratory of New Ceramics and Fine Processing, School of Materials Science and Engineering, Tsinghua University, Beijing 100084, China*

Xian He − *School of Science, Beijing University of Posts and Telecommunications, Beijing 100876, China; State Key Laboratory of New Ceramics and Fine Processing, School of Materials Science and Engineering, Tsinghua University, Beijing 100084, China*

Wei Zhao − *State Key Laboratory of New Ceramics and Fine Processing, School of Materials Science and Engineering, Tsinghua University, Beijing 100084, China*

Hongyi Liu − *Dongfang Electric (Fujian) Innovation Research Institute Co., Ltd., 350108 Chengdu, Fujian Province, China*

Yuanzheng Long − *State Key Laboratory of New Ceramics and Fine Processing, School of Materials Science and Engineering, Tsinghua University, Beijing 100084, China*

Zhuting Zhang − *State Key Laboratory of New Ceramics and Fine Processing, School of Materials Science and Engineering, Tsinghua University, Beijing 100084, China*

Ziwei Li − *State Key Laboratory of New Ceramics and Fine Processing, School of Materials Science and Engineering, Tsinghua University, Beijing 100084, China*

https://doi.org/10.1021/acsnano.4c13787
ACS Nano XXXX, XXX, XXX−XXX

Ke Bi − *School of Science, Beijing University of Posts and Telecommunications, Beijing 100876, China*
Ming Lei − *School of Integrated Circuits, Beijing University of Posts and Telecommunications, Beijing 100876, China;* orcid.org/0000-0001-9818-3586

Complete contact information is available at: https://pubs.acs.org/10.1021/acsnano.4c13787

Author Contributions

H.W., M.L., and K.H. supervised the project. P.D., B.D., K.H., K.B., and H.W. conceived the idea. P.D., X.H., W.Z., Z.Z., Z.L., and K.B. designed the experiment. P.D., B.D., Y.L., H.L., and X.H. carried out the characterization of materials. P.D., K.H., and H.W. contributed to writing the manuscript. All authors discussed the results and commented on the manuscript.

Notes

The authors declare the following competing financial interest(s): A patent for the fabrication method has been applied on behalf of Tsinghua University. H.W., K.H. and P.D. are listed as inventors. Other authors declare that they have no competing financial interests.

ACKNOWLEDGMENTS

This study was supported by the National Natural Science Foundation of China Grant No. 52472087 and 12174154, Basic Science Center Program of the National Natural Science Foundation of China (NSFC) Grant No. 51788104, Fundamental Research Funds for the Central Universities (2023ZCJH03, 2021XD-A041), Fund of State Key Laboratory of Information Photonics and Optical Communications (Beijing University of Posts and Telecommunications, P. R. China), and Teaching Reform Projects at BUPT (2022CXCY-B03).

REFERENCES

(1) Odenweller, A.; Ueckerdt, F.; Nemet, G. F.; Jensterle, M.; Luderer, G. Probabilistic feasibility space of scaling up green hydrogen supply. *Nat. Energy* **2022**, *7* (9), 854−865.
(2) Chen, F.-Y.; Wu, Z.-Y.; Adler, Z.; Wang, H. Stability challenges of electrocatalytic oxygen evolution reaction: From mechanistic understanding to reactor design. *Joule* **2021**, *5* (7), 1704−1731.
(3) Terlouw, T.; Bauer, C.; McKenna, R.; Mazzotti, M. Large-scale hydrogen production via water electrolysis: a techno-economic and environmental assessment. *Energy Environ. Sci.* **2022**, *15* (9), 3583−3602.
(4) Seh, Z. W.; Kibsgaard, J.; Dickens, C. F.; Chorkendorff, I.; Nørskov, J. K.; Jaramillo, T. F. Combining theory and experiment in electrocatalysis: Insights into materials design. *Science* **2017**, *355* (6321), No. eaad4998.
(5) Coughlin, R. W.; Farooque, M. Hydrogen production from coal, water and electrons. *Nature* **1979**, *279* (5711), 301−303.
(6) Wan, L.; Xu, Z.; Xu, Q.; Pang, M.; Lin, D.; Liu, J.; Wang, B. Key components and design strategy of the membrane electrode assembly for alkaline water electrolysis. *Energy Environ. Sci.* **2023**, *16* (4), 1384−1430.
(7) Staffell, I.; Scamman, D.; Abad, A. V.; Balcombe, P.; Dodds, P. E.; Ekins, P.; Shah, N.; Ward, K. R. The role of hydrogen and fuel cells in the global energy system. *Energy Environ. Sci.* **2019**, *12* (2), 463−491.
(8) Selejan, A.-D.; Lisei, H.; Cormos, A.-M.; Dragan, S.; Cormos, C.-C. Development of a multi-scale mathematical model for green hydrogen production via biogas steam reforming process. *Int. J. Hydrogen Energy* **2024**, *52*, 469−484.
(9) Kumar, P.; Date, A.; Mahmood, N.; Das, R. K.; Shabani, B. Freshwater supply for hydrogen production: An underestimated challenge. *Int. J. Hydrogen Energy* **2024**, *78*, 202−217.
(10) Li, Y.; Wei, X.; Chen, L.; Shi, J. Electrocatalytic hydrogen production trilogy. *Angew. Chem., Int. Ed.* **2021**, *60* (36), 19550−19571.
(11) Younas, M.; Shafique, S.; Hafeez, A.; Javed, F.; Rehman, F. An overview of hydrogen production: current status, potential, and challenges. *Fuel* **2022**, *316*, No. 123317.
(12) Logan, B. E.; Shi, L.; Rossi, R. Enabling the use of seawater for hydrogen gas production in water electrolyzers. *Joule* **2021**, *5* (4), 760−762.
(13) Sun, R.; Wang, T.; Yang, X.; Wu, Y.; Wang, Y.; Wu, Q.; Zhang, M.; Brabec, C. J.; Li, Y.; Min, J. High-speed sequential deposition of photoactive layers for organic solar cell manufacturing. *Nat. Energy* **2022**, *7* (11), 1087−1099.
(14) Kim, Y. Y.; Yang, T.-Y.; Suhonen, R.; Kemppainen, A.; Hwang, K.; Jeon, N. J.; Seo, J. Roll-to-roll gravure-printed flexible perovskite solar cells using eco-friendly antisolvent bathing with wide processing window. *Nat. Commun.* **2020**, *11* (1), No. 5146.
(15) Luo, C.; Hu, H.; Zhang, T.; Wen, S.; Wang, R.; An, Y.; Chi, S. S.; Wang, J.; Wang, C.; Chang, J.; et al. Roll-to-roll fabrication of zero-volume-expansion lithium-composite anodes to realize high-energy-density flexible and stable lithium-metal batteries. *Adv. Mater.* **2022**, *34* (38), No. 2205677.
(16) Yang, C.; Ma, H.; Yuan, R.; Wang, K.; Liu, K.; Long, Y.; Xu, F.; Li, L.; Zhang, H.; Zhang, Y.; et al. Roll-to-roll prelithiation of lithium-ion battery anodes by transfer printing. *Nat. Energy* **2023**, *8* (7), 703−713.
(17) Xu, J.; Wu, H.-C.; Zhu, C.; Ehrlich, A.; Shaw, L.; Nikolka, M.; Wang, S.; Molina-Lopez, F.; Gu, X.; Luo, S.; et al. Multi-scale ordering in highly stretchable polymer semiconducting films. *Nat. Mater.* **2019**, *18* (6), 594−601.
(18) Li, Z.; Cui, Z.; Zhao, L.; Hussain, N.; Zhao, Y.; Yang, C.; Jiang, X.; Li, L.; Song, J.; Zhang, B. High-throughput production of kilogram-scale nanofibers by Kármán vortex solution blow spinning. *Sci. Adv.* **2022**, *8* (11), No. eabn3690.
(19) Hansora, D.; Yoo, J. W.; Mehrotra, R.; Byun, W. J.; Lim, D.; Kim, Y. K.; Noh, E.; Lim, H.; Jang, J.-W.; Seok, S. I.; Lee, J. S. All-perovskite-based unassisted photoelectrochemical water splitting system for efficient, stable and scalable solar hydrogen production. *Nat. Energy* **2024**, *9*, 272−284.
(20) Hai, X.; Xi, S.; Mitchell, S.; Harrath, K.; Xu, H.; Akl, D. F.; Kong, D.; Li, J.; Li, Z.; Sun, T.; et al. Scalable two-step annealing method for preparing ultra-high-density single-atom catalyst libraries. *Nat. Nanotechnol.* **2022**, *17* (2), 174−181.
(21) He, X.; Zhang, H.; Zhang, X.; Zhang, Y.; He, Q.; Chen, H.; Cheng, Y.; Peng, M.; Qin, X.; Ji, H.; Ma, D. Building up libraries and production line for single atom catalysts with precursor-atomization strategy. *Nat. Commun.* **2022**, *13* (1), No. 5721.
(22) Li, F.; Yang, H.; Li, W.; Sun, L. Device fabrication for water oxidation, hydrogen generation, and CO_2 reduction via molecular engineering. *Joule* **2018**, *2* (1), 36−60.
(23) Tao, L.; Lv, F.; Wang, D.; Luo, H.; Lin, F.; Gong, H.; Mi, H.; Wang, S.; Zhang, Q.; Gu, L.; et al. Mass-efficient catalyst layer of hierarchical sub-nanosheets on nanowire for practical proton exchange membrane electrolyzer. *Joule* **2024**, *8* (2), 450−460.
(24) Yu, Q.; Zhang, Z.; Qiu, S.; Luo, Y.; Liu, Z.; Yang, F.; Liu, H.; Ge, S.; Zou, X.; Ding, B.; et al. A Ta-TaS_2 monolith catalyst with robust and metallic interface for superior hydrogen evolution. *Nat. Commun.* **2021**, *12* (1), No. 6051.
(25) Wang, S.; Lu, A.; Zhong, C.-J. Hydrogen production from water electrolysis: role of catalysts. *Nano Convergence* **2021**, *8* (1), 4.
(26) Holmes-Gentle, I.; Tembhurne, S.; Suter, C.; Haussener, S. Kilowatt-scale solar hydrogen production system using a concentrated integrated photoelectrochemical device. *Nat. Energy* **2023**, *8* (6), 586−596.
(27) Sun, H.; Xu, X.; Kim, H.; Jung, W.; Zhou, W.; Shao, Z. Electrochemical water splitting: Bridging the gaps between fundamental research and industrial applications. *Energy Environ. Mater.* **2023**, *6* (5), No. e12441.
(28) Chatenet, M.; Pollet, B. G.; Dekel, D. R.; Dionigi, F.; Deseure, J.; Millet, P.; Braatz, R. D.; Bazant, M. Z.; Eikerling, M.; Staffell, I.; et al. Water electrolysis: from textbook knowledge to the latest scientific

strategies and industrial developments. *Chem. Soc. Rev.* **2022**, *51* (11), 4583−4762.
(29) Qin, X.; Xu, M.; Guan, J.; Feng, L.; Xu, Y.; Zheng, L.; Wang, M.; Zhao, J.-W.; Chen, J.-L.; Zhang, J.; et al. Direct conversion of CO and H_2O to hydrocarbons at atmospheric pressure using a TiO_{2-x}/Ni photothermal catalyst. *Nat. Energy* **2024**, *9*, 154−162.
(30) Yuan, S.; Peng, J.; Cai, B.; Huang, Z.; Garcia-Esparza, A. T.; Sokaras, D.; Zhang, Y.; Giordano, L.; Akkiraju, K.; Zhu, Y. G.; et al. Tunable metal hydroxide-organic frameworks for catalysing oxygen evolution. *Nat. Mater.* **2022**, *21* (6), 673−680.
(31) Dong, Q.; Lele, A. D.; Zhao, X.; Li, S.; Cheng, S.; Wang, Y.; Cui, M.; Guo, M.; Brozena, A. H.; Lin, Y.; et al. Depolymerization of plastics by means of electrified spatiotemporal heating. *Nature* **2023**, *616* (7957), 488−494.
(32) Luong, D. X.; Bets, K. V.; Algozeeb, W. A.; Stanford, M. G.; Kittrell, C.; Chen, W.; Salvatierra, R. V.; Ren, M.; McHugh, E. A.; Advincula, P. A.; et al. Gram-scale bottom-up flash graphene synthesis. *Nature* **2020**, *577* (7792), 647−651.
(33) Dong, Q.; Yao, Y.; Cheng, S.; Alexopoulos, K.; Gao, J.; Srinivas, S.; Wang, Y.; Pei, Y.; Zheng, C.; Brozena, A. H.; et al. Programmable heating and quenching for efficient thermochemical synthesis. *Nature* **2022**, *605* (7910), 470−476.
(34) Kim, Y. T.; Lee, J.-J.; Lee, J. Electricity-driven reactors that promote thermochemical catalytic reactions via joule and induction heating. *Chem. Eng. J.* **2023**, *470*, No. 144333, DOI: 10.1016/j.cej.2023.144333.
(35) Liu, S.; Hu, Z.; Wu, Y.; Zhang, J.; Zhang, Y.; Cui, B.; Liu, C.; Hu, S.; Zhao, N.; Han, X.; et al. Dislocation-strained IrNi alloy nanoparticles driven by thermal shock for the hydrogen evolution reaction. *Adv. Mater.* **2020**, *32* (48), No. 2006034.
(36) Yao, Y.; Huang, Z.; Xie, P.; Wu, L.; Ma, L.; Li, T.; Pang, Z.; Jiao, M.; Liang, Z.; Gao, J.; et al. High temperature shockwave stabilized single atoms. *Nat. Nanotechnol.* **2019**, *14* (9), 851−857.
(37) Yao, Y.; Huang, Z.; Xie, P.; Lacey, S. D.; Jacob, R. J.; Xie, H.; Chen, F.; Nie, A.; Pu, T.; Rehwoldt, M.; et al. Carbothermal shock synthesis of high-entropy-alloy nanoparticles. *Science* **2018**, *359* (6383), 1489−1494.
(38) Wu, H.; Lu, Q.; Li, Y.; Wang, J.; Li, Y.; Jiang, R.; Zhang, J.; Zheng, X.; Han, X.; Zhao, N.; et al. Rapid joule-heating synthesis for manufacturing high-entropy oxides as efficient electrocatalysts. *Nano Lett.* **2022**, *22* (16), 6492−6500.
(39) Li, C.; Wang, Z.; Liu, M.; Wang, E.; Wang, B.; Xu, L.; Jiang, K.; Fan, S.; Sun, Y.; Li, J.; Liu, K. Ultrafast self-heating synthesis of robust heterogeneous nanocarbides for high current density hydrogen evolution reaction. *Nat. Commun.* **2022**, *13* (1), No. 3338.
(40) Xu, F.; Zhou, Y.; Zhai, X.; Zhang, H.; Liu, H.; Ang, E. H.; Lu, Y.; Nie, Z.; Zhou, M.; Zhu, J. Ultrafast universal fabrication of metal-organic complex nanosheets by joule heating engineering. *Small Methods* **2022**, *6* (1), No. 2101212.
(41) Han, Y.-C.; Liu, M.-L.; Sun, L.; Li, S.; Li, G.; Song, W.-S.; Wang, Y.-J.; Nan, Z.-A.; Ding, S.-Y.; Liao, H.-G.; et al. A general method for rapid synthesis of refractory carbides by low-pressure carbothermal shock reduction. *Proc. Natl. Acad. Sci. U.S.A.* **2022**, *119* (37), No. e2121848119.
(42) He, X.; Du, P.; Yu, G.; Wang, R.; Long, Y.; Deng, B.; Yang, C.; Zhao, W.; Zhang, Z.; Huang, K.; et al. High-performance hydrogen evolution reaction catalytic electrodes by liquid Joule-heating growth. *Small Methods* **2023**, *7* (11), No. 2300544.
(43) Li, G.; Zhang, W.; Nie, K.; Lv, X.; Deng, J.; Ji, H. Flash Joule heating to enhance water oxidation of hematite photoanode via mediating with an oxidized carbon overlayer. *Carbon* **2023**, *215*, No. 118444.
(44) Mei, X.; Zhu, X.; Zhang, Y.; Zhang, Z.; Zhong, Z.; Xin, Y.; Zhang, J. Decreasing the catalytic ignition temperature of diesel soot using electrified conductive oxide catalysts. *Nat. Catal.* **2021**, *4* (12), 1002−1011.
(45) Zhu, Q.; Li, H.; Wang, Y.; Zhou, Y.; Zhu, A.; Chen, X.; Li, X.; Chen, Y.; Lu, H. Novel metallic electrically heated monolithic catalysts towards VOC combustion. *Catal. Sci. Technol.* **2019**, *9* (23), 6638−6646.
(46) Dionigi, F.; Zeng, Z.; Sinev, I.; Merzdorf, T.; Deshpande, S.; Lopez, M. B.; Kunze, S.; Zegkinoglou, I.; Sarodnik, H.; Fan, D.; et al. In-situ structure and catalytic mechanism of NiFe and CoFe layered double hydroxides during oxygen evolution. *Nat. Commun.* **2020**, *11* (1), No. 2522.
(47) Lee, H. S.; Shin, H.; Park, S.; Kim, J.; Jung, E.; Hwang, W.; Lee, B.-H.; Yoo, J. M.; Antink, W. H.; Lee, K.; et al. Electrochemically generated electrophilic peroxo species accelerates alkaline oxygen evolution reaction. *Joule* **2023**, *7* (8), 1902−1919.
(48) Zhao, W.; Xu, H.; Luan, H.; Chen, N.; Gong, P.; Yao, K.; Shen, Y.; Shao, Y. NiFe layered double hydroxides grown on a corrosion-cell cathode for oxygen evolution electrocatalysis. *Adv. Energy Mater.* **2022**, *12* (2), No. 2102372.
(49) He, Z.; Zhang, J.; Gong, Z.; Lei, H.; Zhou, D.; Zhang, N.; Mai, W.; Zhao, S.; Chen, Y. Activating lattice oxygen in NiFe-based (oxy)hydroxide for water electrolysis. *Nat. Commun.* **2022**, *13* (1), No. 2191.
(50) Zhang, B.-J.; Chang, B.; Qiu, S.-P.; Zhao, G.; Wang, X.; Xu, X.-J.; Mu, L.; Liao, W.-B.; Dong, X.-J. Two-dimensional bifunctional electrocatalyst (Mo−NiFe-LDH) with multilevel structure for highly efficient overall water splitting. *Rare Met.* **2024**, *43* (6), 2613−2622.
(51) Dai, J.; Zhang, Y.; Song, H.; Liu, L. NiFe layered-double-hydroxide nanosheet arrays grown in situ on Ni foam for efficient oxygen evolution reaction. *Int. J. Hydrogen Energy* **2024**, *87*, 130−137.
(52) Zhang, L.; Peng, L.; Lu, Y.; Ming, X.; Sun, Y.; Xu, X.; Xia, Y.; Pang, K.; Fang, W.; Huang, N.; et al. Sub-second ultrafast yet programmable wet-chemical synthesis. *Nat. Commun.* **2023**, *14* (1), No. 5015.
(53) Iwata, R.; Zhang, L.; Wilke, K. L.; Gong, S.; He, M.; Gallant, B. M.; Wang, E. N. Bubble growth and departure modes on wettable/non-wettable porous foams in alkaline water splitting. *Joule* **2021**, *5* (4), 887−900.
(54) Li, N.; Cai, L.; Gao, G.; Lin, Y.; Wang, C.; Liu, H.; Liu, Y.; Duan, H.; Ji, Q.; Hu, W.; et al. Operando Direct Observation of Stable Water-Oxidation Intermediates on $Ca_{2-x}IrO_4$ Nanocrystals for Efficient Acidic Oxygen Evolution. *Nano Lett.* **2022**, *22* (17), 6988−6996.
(55) Liang, C.; Rao, R. R.; Svane, K. L.; Hadden, J. H. L.; Moss, B.; Scott, S. B.; Sachs, M.; Murawski, J.; Frandsen, A. M.; Riley, D. J.; et al. Unravelling the effects of active site density and energetics on the water oxidation activity of iridium oxides. *Nat. Catal.* **2024**, *7* (7), 763−775.
(56) Zhao, G.; Li, P.; Cheng, N.; Dou, S. X.; Sun, W. An Ir/$Ni(OH)_2$ Heterostructured Electrocatalyst for the Oxygen Evolution Reaction: Breaking the Scaling Relation, Stabilizing Iridium(V), and Beyond. *Adv. Mater.* **2020**, *32* (24), No. 2000872.
(57) Liu, T.; Zhao, Y.; Zhai, T. Does a Higher Density of Active Sites Indicate a Higher Reaction Rate? *J. Am. Chem. Soc.* **2024**, *146* (10), 6461−6465.
(58) Wang, J.; Liang, C.; Ma, X.; Liu, P.; Pan, W.; Zhu, H.; Guo, Z.; Sui, Y.; Liu, H.; Liu, L.; Yang, C. Dynamically adaptive bubbling for upgrading oxygen evolution reaction using lamellar fern-like alloy aerogel self-standing electrodes. *Adv. Mater.* **2024**, *36* (1), No. 2307925.
(59) Lu, S.-Y.; Huang, B.; Sun, M.; Luo, M.; Jin, M.; Yang, H.; Zhang, Q.; Liu, H.; Zhou, P.; Chao, Y.; et al. Synthetic tuning stabilizes a high-valence Ru single site for efficient electrolysis. *Nat. Synth.* **2024**, *3*, 576−585.
(60) Hu, X.; Hu, B.; Niu, C.; Yao, J.; Liu, M.; Tao, H.; Huang, Y.; Kang, S.; Geng, K.; Li, N. An operationally broadened alkaline water electrolyser enabled by highly stable poly(oxindole biphenylene) ion-solvating membranes. *Nat. Energy* **2024**, *9*, 401−410, DOI: 10.1038/s41560-023-01447-w.
(61) Wallace, A. G.; Symes, M. D. Decoupling strategies in electrochemical water splitting and beyond. *Joule* **2018**, *2* (8), 1390−1395.
(62) Zuo, Y.; Bellani, S.; Saleh, G.; Ferri, M.; Shinde, D. V.; Zappia, M. I.; Buha, J.; Brescia, R.; Prato, M.; Pascazio, R.; et al. Ru-Cu Nanoheterostructures for Efficient Hydrogen Evolution Reaction in

Alkaline Water Electrolyzers. *J. Am. Chem. Soc.* **2023**, *145* (39), 21419−21431.
(63) Ling, S.; Li, X.; Zhou, T.; Yuan, R.; Sun, S.; He, H.; Zhang, C. Densifiable ink extrusion for roll-to-roll fiber lithium-ion batteries with ultra-high linear and volumetric energy densities. *Adv. Mater.* **2023**, *35* (14), No. 2211201.
(64) Liu, Y.; Gong, X.; Podder, C.; Wang, F.; Li, Z.; Liu, J.; Fu, J.; Ma, X.; Vanaphuti, P.; Wang, R.; et al. Roll-to-roll solvent-free manufactured electrodes for fast-charging batteries. *Joule* **2023**, *7* (5), 952−970.
(65) Zeng, L.; Chen, Y.; Sun, M.; Huang, Q.; Sun, K.; Ma, J.; Li, J.; Tan, H.; Li, M.; Pan, Y.; et al. Cooperative Rh-O_5/Ni (Fe) site for efficient biomass upgrading coupled with H_2 production. *J. Am. Chem. Soc.* **2023**, *145* (32), 17577−17587.
(66) Lu, Y.; Liu, T.; Huang, Y.-C.; Zhou, L.; Li, Y.; Chen, W.; Yang, L.; Zhou, B.; Wu, Y.; Kong, Z.; et al. Integrated catalytic sites for highly efficient electrochemical oxidation of the aldehyde and hydroxyl groups in 5-hydroxymethylfurfural. *ACS Catal.* **2022**, *12* (7), 4242−4251.
(67) Robb, B. H.; Farrell, J. M.; Marshak, M. P. Chelated chromium electrolyte enabling high-voltage aqueous flow batteries. *Joule* **2019**, *3* (10), 2503−2512.

https://doi.org/10.1021/acsnano.4c13787
ACS Nano XXXX, XXX, XXX−XXX